Heliyon 9 (2023) e20710

Contents lists available at ScienceDirect

Heliyon

journal homepage: www.cell.com/heliyon

New hybrid radio-fluorescent probes [^{131}I]-BPF-01 and [^{131}I]-BPF-02 for visualisation of cancer cells: Synthesis and preliminary in vitro and ex vivo evaluations

Hendris Wongso [a,b,*], Ahmad Kurniawan [a], Alfian M. Forentin [a], Veronika Y. Susilo [a], Yanuar Setiadi [c], Isa Mahendra [a,b], Muhamad B. Febrian [a], Aziiz M. Rosdianto [d,e], Iwan Setiawan [d,e], Hanna Goenawan [d,e], Susianti Susianti [f], Unang Supratman [f,g], Eva M. Widyasari [a], Teguh H.A. Wibawa [a], Maula E. Sriyani [a], Iim Halimah [a], Ronny Lesmana [d,e,**]

[a] *Research Center for Radioisotope, Radiopharmaceutical, and Biodosimetry Technology, Research Organization for Nuclear Energy, National Research and Innovation Agency, Puspiptek, Banten, 15314, Indonesia*
[b] *Research Collaboration Center for Theranostic Radiopharmaceuticals, National Research and Innovation Agency, Jl. Raya Bandung-Sumedang KM 21, Sumedang, 45363, Indonesia*
[c] *Research Center for Environmental and Clean Technology, Research Organization for Life Sciences and Environment, National Research and Innovation Agency, Puspiptek, Banten, 15314, Indonesia*
[d] *Department of Biomedical Science, Physiology Division, Faculty of Medicine, Universitas Padjadjaran, Jatinangor, 45363, Indonesia*
[e] *Laboratory of Sciences, Graduate School, Universitas Padjadjaran, Bandung, Indonesia*
[f] *Central Laboratory, Universitas Padjadjaran, Jatinangor 45363, Indonesia*
[g] *Department of Chemistry, Faculty of Mathematics and Natural Sciences, Universitas Padjadjaran, Jatinangor 45363, Indonesia*

ARTICLE INFO

Keywords:
Fluorescent
Hybrid radio-fluorescent
Solid cancers
Imaging
Image-guided surgery

ABSTRACT

We synthesised and biologically evaluated two new hybrid probes **[^{131}I] BPF-01** and **[^{131}I] BPF-02** which were built from three structural entities: benzothiazole-phenyl, fluorescein isothiocyanate (FITC), and iodine-131. These probes were designed for potential applications in assisting surgical procedures of solid cancers. The cytotoxicity study demonstrated that fluorescent probes **BPF-01** (31.23 μg/mL) and **BPF-02** (250 μg/mL) were relatively not toxic to normal immortalized human keratinocytes (HaCaT) cells, as indicated by the percentage of cell survival above 50 %. Furthermore, both probes displayed low to moderate anticancer activity against the breast cancer cells (MDA-MB-231) and prostate cancer cells (LNCaP and DU-145). The probe **BPF-01** apparently showed an accumulation in the tumour tissues, as suggested by ex vivo fluorescence examinations. In addition, the cellular uptake study suggests that hybrid probe **[^{131}I] -BPF-01** was potentially accumulated in the MCF-7 cell line with the highest uptake of 16.11 ± 1.52 % after 2 h of incubation, approximately 50-fold higher than the accumulation of iodine-131 (control). The magnetic bead assay suggests that **[^{131}I] -BPF-02** and **[^{131}I] -BPF-02** showed a promising capability to interact with translocator protein 18 kDa (TSPO). Moreover, the computational data

* Corresponding author. Research Center for Radioisotope, Radiopharmaceutical, and Biodosimetry Technology, Research Organization for Nuclear Energy, National Research and Innovation Agency, Puspiptek, Banten, 15314, Indonesia.

** Corresponding author. Department of Biomedical Science, Physiology Division, Faculty of Medicine, Universitas Padjadjaran, Jatinangor 45363, Indonesia.

E-mail addresses: hend042@brin.go.id (H. Wongso), ronny@unpad.ac.id (R. Lesmana).

https://doi.org/10.1016/j.heliyon.2023.e20710
Received 30 April 2023; Received in revised form 30 September 2023; Accepted 4 October 2023
Available online 5 October 2023

showed that the binding scores for ligands **7**–**8**, **BPF-01** and **BPF-02**, and **[^{131}I]-BPF-01** and **[^{131}I]-BPF-02** in the TSPO were considerably high. Accordingly, fluorescent probes **BPF-01** and **BPF-02**, and hybrid probes **[^{131}I] BPF-01** and **[^{131}I] BPF-02** can be further developed for targeting cancer cells during intraoperative tumour surgery.

1. Introduction

Cancer is a major health problem which is correlated with a huge economic burden for the community [1,2]. It is reported that about 19.3 million new cases and a total of 10.0 million deaths occurred in 2020 on a global scale [3]. Generally, tumour diagnosis can be achieved using a number of anatomical and functional imaging tools, including magnetic resonance imaging (MRI) computed tomography (CT), single-photon emission computed tomography (SPECT), and positron emission tomography (PET). However, most parts of these techniques can not be used for intraoperative detection of tumours, for example, for guiding tumour resection [4].

Over the past few decades, available treatments to remove cancers include surgery, chemotherapy, and radiation therapy, however, significant advances have been made in recent years to provide better treatments employing sonodynamic and chemodynamic, stem cell, and ferroptosis-based therapy [5]. The application of surgery alone in clinical settings or combined with radiotherapy is one of the most recommended approaches for various cancers, particularly solid tumours [5,6]. The main goal of surgical procedure is to achieve a complete removal of cancerous cells/tissues, resulting in a negative surgical margin (NSM) [7,8]. Although surgical resection of the primary tumour or metastatic lesions can lead to a positive outcome for patients, it has long been indicated that the surgical insult itself (e.g., tissue trauma caused by sterile dissection), in some cases, could elicit a cascade of local and systemic inflammation, resulting to an acceleration of the tumour recurrence and metastatic growth [9].

Several reports have suggested that the use of radioguided surgery (RGS) may help surgeons distinguish between malignancy and non-malignancy tissues as well as verify surgical margins. During RGS, the surgeon uses a handheld radiation detector to navigate tumour tissues that have been tagged with a radiolabelled compound [10]. On the other hand, tumour surgery assisted by fluorescence guidance, widely recognised as fluorescence image-guided surgery (FIGS) has also attracted scientists' interest. FIGS offers a new intraoperative strategy to improve clinical surgery outcomes by accurately visualising cancer cells, defining tumour-positive margins, and locating metastases [11,12].

Although radioactive probe offers high tissue penetration and high-sensitivity imaging [13,14], the use of this modality alone is often associated with a high-cost procedure as a result of expensive instrumentations and equipment [15]. Moreover, the application of fluorescent imaging offers several advantages (e.g., low cost of instrumentations and portability and real-time capabilities). Nevertheless, its widespread use is limited by light scattering and low tissue penetration [16,17]. To overcome these issues, several probes containing hybrid radioactive material and fluorescent agents have been developed, inspired by the fact that these two modalities could provide complementary imaging information. Accumulating evidence has shown that the application of hybrid probes successfully leads to improved clinical outcomes [15,18,19]. The main advantage of this technology is the hybrid tracers allow simultaneous preoperative whole-body imaging, followed by image-guided surgery of tumour.

Here, we reported the discovery of two novel hybrid molecules bearing benzothiazole (BTA) skeleton, radionuclide iodine-131, and fluorescein isothiocyanate (FITC) fluorophore, namely **[^{131}I]-BPF-01** and **[^{131}I]-BPF-02**. BTA was selected as this scaffold has been reported to possess several pharmacological actions [20]. Moreover, our previous study has revealed that a BTA-containing fluorescent probe exhibited potential binding to cancer cells [21]. The FITC was chosen as the fluorophore because it exhibits favourable chemical properties, including water soluble, good photostability and biocompatibility, and relatively high fluorescence emission intensity [22]. The synthesised fluorescent probes **BPF-01** and **BPF-02** can potentially be used for ex vivo imaging, detection of tumour residue, and tissues biopsy examination of the solid tumour during the surgery, while their corresponding fluorescent-radioactive probes (**[^{131}I]-BPF-01** and **[^{131}I]-BPF-02**) can be utilised as radiotracers to navigate the precise location of tumour tissues and surgical margin using a handheld gamma detector.

2. Experimental

2.1. Materials and instruments

The chemicals used for this research were of analytical grade, and purchased from Merck Singapore, unless stated otherwise. The high purity solvents (HPLC-grade) were used for the reactions and purification of compounds. Monitoring of reaction was accomplished by thin-layer chromatography (TLC) with aluminium-back silica gel sheets (F_{254}; 0.20 mm thickness), assisted with UV lamp using the wavelengths (λ) of254 and 365 nm. The removal of solvent residues was performed via concentration under low pressure using DLAB RE100-Pro rotavapor. The purification of synthesised compounds/intermediates was realised by preparative chromatography on TLC plates (silica gel 60 F_{254} 1 mm, 20 × 20 cm^2). The measurement of the proton (^{1}H)- and carbon (^{13}C) nuclear magnetic resonance (NMR) spectra was performed on a JEOL-ECZ 500R (500 MHz). The mass spectrometry spectra were obtained using a mass spectrometer (Water Q-Tof MS Xevo) on (+) and (−) electrospray ionisation modes. The measurement of infrared spectroscopy (IR) spectra was accomplished using an ALPHA FT-IR Spectrometer Bruker. The ultraviolet (UV)-visible data were obtained at room temperature (±23 °C) on a JASCO V-550 UV-VIS spectrophotometer. The purity of the compounds was investigated by the high-performance liquid chromatography (HPLC) on 1260 Infinity G1314F Agilent, with a stationary phase of 5 μm, 4.6 × 150 mm C18

Eclipse XDB column. The isocratic method with two mobile phases: 0.1 % trifluoracetic acid (TFA) in H_2O 50 % (A), and 0.1 % TFA in acetonitrile 50 % (B) with a running time of 30 min, and a moderate flow rate (1.0 mL/min) at 25 °C was used. The purity of the synthesised fluorescent probes BPF-01 and BPF-02 was found to be 100 %.

2.2. Synthesis of probes BPF-01 and BPF-02

2.2.1. General procedure A: synthesis of amides

The imidazopyridine carboxylic acid (1.0 eq), the mono-*N*-Boc-protected amine (1.2 eq), EDCI (1.3 eq), HOBT (1.0 eq), and *N*,*N*-Diisopropylethylamine (DIPEA) (4.0 eq) were added to dry DMF (6.0 mL/mmol acid), and then incubated with stirring at rt for 24 h under N_2. Subsequently, the solution was combined into H_2O (15 mL) and then partitioned with ethyl acetate (2 × 15 mL). The ethyl acetate fraction was rinsed with H_2O (2 × 15 mL) and brine (15 mL), dried using sodium sulfate, filtered, and concentrated with a rotavapor. The crude residue was transferred to a preparative TLC (CH_2Cl_2/MeOH – 90:10) to yield the corresponding amides **5**–**6**.

2.2.2. General procedure B: synthesis of target probes

To an appropriate amine **5** or **6** in CH_2Cl_2 (2.0 mL) was slowly added TFA solution (0.5 mL) at 0 °C. The substances were stirred at rt for 18 h, and the solvents were removed using a stream of N_2 over 5 min. To the solid residue was added toluene (20 mL) to remove the excess TFA. This step was repeated twice to give the corresponding amine **7** or **8**. The free amine (approximately 1 eq) was then added to anhydrous DMF (1.5 mL), and then placed into an ice bath. DIPEA (2 eq) was gently added to the reaction under N_2, followed by slow addition of DMF (1.5 mL) containing FITC (1.1 eq). Then, the reaction vessel (round bottom flask) was protected from light with aluminum foil and incubated for 18 h. To the resulting solution was slowly added H_2O (25 mL), followed by EtOAc (25 mL), and then partitioned. The H_2O fraction was further extracted using EtOAc (2 × 25 mL). The EtOAc fractions were collected, and then washed again twice with H_2O (2 × 50 mL) and brine (50 mL), and dried using sodium sulfate. The concentrate was dried on a rotavapor. The solid residue was transferred to a preparative TLC (CH_2Cl_2/MeOH – 90:10) to afford final probes **BPF-01** and **BPF-02**.

2.2.3. Compound **5** [21]

As outlined in Procedure A, carboxylic acid **2** (199 mg, 0.95 mmol), *tert*-butyl (4-aminobenzyl)carbamate (211 mg, 0.95 mmol) **3**, EDCI (239 mg, 1.05 mmol), HOBT (141 mg, 0.95 mmol), and DIPEA (0.33 mL, 1.90 mmol) were combined and stirred to generate the amide **5** (300 mg, 77 %) as a white-off solid. The spectroscopic data were identical with a previous report.

2.2.4. Compound **6**

As outlined in Procedure A, carboxylic acid **2** (199 mg, 0.95 mmol), *tert*-butyl (4-aminobenzyl)carbamate (224 mg, 0.95 mmol) **4**, EDCI (239 mg, 1.05 mmol), HOBT (141 mg, 0.95 mmol), and DIPEA (0.33 mL, 1.90 mmol) were combined and stirred to generate the amide **6** (290 mg, 71 %) as a white-off solid. TLC (MeOH/CH_2Cl_2-10:90): $R_f = 0.68$.^{1}H NMR (500 MHz, DMSO-d_6) δ 10.94 (s, 1H), 8.08 (d, $J = 10.0$ Hz, 1H), 7.81–7.79 (m, 3H), 7.25 (dd, $J = 2.5$, 10 Hz, 1H), 7.19 (d, $J = 10.0$ Hz, 1H), 6.89 (d, $J = 5.0$ Hz, 1H), 3.88 (s, 3H), 3.14 (m, 2H), 2.67 (t, $J = 5.0$ Hz, 2H), 1.37 (s, 9H). ^{13}C NMR (500 MHz, DMSO-d_6) δ 161.9, 158.7, 158.1, 155.5, 147.1, 138.3, 136.1, 135.6, 128.9, 124.8, 120.7, 117.4, 104.8, 77.5, 55.9, 41.5, 35.0, 28.3. IR (neat)max 3376 (w), 2972 (w), 2929 (w), 1701 (s), 1669 (s), 1595 (m), 1533 (s), 1514 (s), 1491 (s), 1454 (m), 1433 (m), 1415 (m), 1242 (s), 1222 (m), 1224 (s), 1164 (s), 1128 (s), 1090 (s), 1052 (m), 989 (m), 908 (m), 840 (s), 821 (m), 654 (m), 635 (m), 599 (m), 571 (m), 509 (s) cm-1. HRMS (ESI + ve TOF) for $C_{22}H_{26}N_3O_4S^+$ 428.1639, observed 428.1656 ($[M+H]^+$).

2.2.5. Fluorescent probe **BPF-01**

As outlined in Procedure B, amide **5** (100 mg, 0.24 mmol) in DCM (2 mL):TFA (0.5 mL) was incubated with stirring to afford the TFA salt 7 (98 mg, 90 %) as a brown solid. TLC (MeOH/CH_2Cl_2-10:90): $R_f = 0.44$. The salt (98 mg, 0.22 mmol), FITC (85 mg, 0.22 mmol), and DIPEA (0.17 mL, 0.85 mmol) were stirred to afford fluorescent probe **BPF-01** (81 mg, 52 %) as an orange solid after preparative TLC. TLC (MeOH/CH_2Cl_2-10:90): $R_f = 0.44$.^{1}H NMR (500 MHz, DMSO-d_6) δ 10.16 (br s, 2H), 8.12 (br s, 2H), 8.05 (d, $J =$ 10 Hz, 1H), 7.99–8.00 (m, 1H), 7.89 (d, $J = 5.0$ Hz, 1H), 7.76–7.79 (m, 2H), 7.42 (d, $J = 10$ Hz, 2H), 7.31 (d, $J = 10$ Hz, 1H), 7.22 (dd, J = 5.0, 10 Hz, 1H), 6.64 (d, $J = 5.0$ Hz, 2H), 6.56–6.58 (m, 3H), 6.50–6.52 (m, 3H), 3.97–4.00 (m, 2H), 3.84 (s, 3H). ^{13}C NMR (500 MHz, DMSO-d_6) δ 169.0, 167.9, 162.1, 162.0, 160.2, 160.0, 159.3, 158.9, 152.4, 151.4, 147.6, 138.9, 138.7, 133.9, 132.6, 130.3, 130.0, 129.7, 128.3, 126.2, 125.4, 124.5, 122.3, 121.3, 113.2, 110.1, 109.4, 106.4, 102.8, 56.4, 42.5. IR $(neat)_{max}$ 3387 (w), 2922 (w), 2852 (w), 1649 (s), 1593 (m), 1557 (m), 1437 (m), 1411 (m), 1384 (s), 1306 (m), 1255 (m), 1197 (m), 1172 (m), 1100 (s), 972 (m), 914 (m), 846 (m), 800 (m), 721 (m), 661 (m), 596 (m), 571 (m) cm^{-1}. HRMS (ESI-ve TOF) for $C_{37}H_{25}N_4O_7S_2^-$ 701.1170, observed 701.1169 ($[M - H]^-$).

2.2.6. Fluorescent probe **BPF-02**

As outlined in Procedure B, amide **6** (103 mg, 0.24 mmol) in DCM (2 mL):TFA (0.5 mL) was incubated with stirring to afford the TFA salt 8 (90 mg, 81 %) as a brown solid. TLC (MeOH/CH_2Cl_2-10:90): $R_f = 0.43$. The salt (90 mg, 0.19 mmol), FITC (76 mg, 0.19 mmol), and DIPEA (0.17 mL, 0.85 mmol) were stirred to afford fluorescent probe **BPF-01** (77 mg, 57 %) as an orange solid after preparative TLC. TLC (MeOH/CH_2Cl_2-10:90): $R_f = 0.42$.^{1}H NMR (500 MHz, DMSO-d_6) δ 10.29 (br s, 2H), 8.37 (d, $J = 5.0$ Hz, 1H), 7.96 (dd, $J = 5.0$, 10 Hz, 1H), 7.88 (d, $J = 10$ Hz, 1H), 7.60 (d, $J = 5.0$ Hz, 2H), 7.53 (d, $J = 5.0$ Hz, 2H), 7.40–7.43 (m, 1H), 7.21–7.23 (m, 1H), 7.09 (dd, $J = 5.0$, 10 Hz, 2H), 6.88 (d, $J = 10$ Hz, 2H), 6.70 (d, $J = 5.0$ Hz, 2H), 6.57–6.59 (m, 2H), 6.48 (d, $J = 10$ Hz, 2H), 4.12 (m, 2H), 3.93 (m, 2H), 3.84 (s, 3H). ^{13}C NMR (500 MHz, DMSO-d_6) δ 179.7, 168.7, 162.7, 159.6, 157.7, 155.8, 155.7, 151.9, 147.8,

147.4, 141.9, 138.1, 136.5, 129.1, 128.0, 127.2, 127.0, 126.4, 124.4, 124.0, 117.4, 115.7, 113.7, 112.7, 109.7, 104.4, 102.3, 77.8, 77.5, 55.7, 43.2, 43.1. IR $(neat)_{max}$ 3233 (w), 2918 (w), 1736 (w), 1654 (m), 1638 (m), 1584 (m), 1458 (s), 1407 (m), 1382 (m), 1302 (m), 1245 (m), 1206 (m), 1172 (s), 1107 (s), 992 (m), 911 (m), 844 (m), 785 (m), 712 (m), 662 (m), 597 (m), 571 (m) cm^{-1}. HRMS (ESI-ve TOF) for $C_{38}H_{27}N_4O_7S_2^-$ 715.1327, observed 715.1325 ($[M - H]^-$).

2.3. Ultraviolet–visible (UV–Vis) analysis

To the probe **BPF-01**/**BPF-02** was added dimethyl sulfoxide (DMSO). The sample solution was then diluted into a concentration of 10 μM for every experiment. A concentration of DMSO below 1.0 % (v/v) solutions was used for all assay solutions. Briefly, the UV spectra were measured from 11 different ratios of dioxane in phosphate-buffered saline (PBS) (0, 10, 20, 30, 40, 50, 60, 70, 80, 90, and 100 % dioxane) using a UV–visible spectrophotometer.

2.4. Cell lines

HaCaT (primary epidermal keratinocytes) cell line was purchased from ATCC as a normal cell model, MDA-MB-231 was obtained from ATCC as a triple-negative breast cancer cell line, and LNCaP and DU-145 were purchased from ECACC and ATCC, respectively, as prostate cancer cell lines. Human breast cancer cell MCF-7 (HTB-22) and human lung cancer cell A549 (CCL-185) were obtained from ATCC. Cells were cultured and maintained in the RPMI 1640 medium containing 10 % fetal bovine serum (Gibco), 10 mM sodium pyruvate (Gibco), streptomycin (100 μg/mL), penicillin (100 units/mL) (Sigma Aldrich), and amphotericin B (2.5 μg/mL) (Gibco), and incubated in a humidifies atmosphere (5 % CO_2 with 90 % humidity) at 37 °C in a CO_2 incubator.

2.5. Biocompatibility and anticancer assays

Each test sample (**BPF-01** and **BPF-02**) was prepared by dissolving with 0.5 % DMSO in the complete growth medium and vigorously shaking to ensure uniform solution dispersion. All studied cell lines were treated with progressively doubling concentrations starting from 0.0156 to 0.5000 mg/mL. Conversely, cisplatin and docetaxel were used as positive controls for cytotoxic agents. There were two groups of control cells: those grown in the presence of DMSO and without DMSO. Both biocompatibility and anticancer properties of the samples were evaluated using 3-(4,5-dimethylthiazol-2-yl)-2,5-di-phenyl-2H-tetrazolium bromide (MTT) method as previously reported by Mossman [23], with minor modifications. Briefly, the cells (1×10^4 cells/well) were seeded in 96-well microplates (flat bottoms). After reaching 80 % confluence, cells were incubated with the samples for 24 h, as outlined in the section on treatments. The growth medium was withdrawn after incubation. Subsequently, the remaining cells were rinsed twice with cold PBS. Each well, including the control groups, received 100 μL of medium supplemented with the MTT reagent to obtain a concentration of 0.5 mg/mL. The cells were further incubated in 5 % CO_2 at 37 °C for 2–4 h. After the formation of formazan crystal, 100 μL of 10 % SDS solution was added. A microplate reader was used to determine the cell viability by measuring absorbance at 570 nm. For the study of the anticancer effect of **BPF-01** against LNCaP, the study was carried out using the resazurin reduction assay, following a previously report [21].

2.6. Animals

The use of mice in this study has been reviewed and approved by the Institutional Ethical Clearance and Foreign Research Permit of the National Research and Innovation Agency of the Republic of Indonesia (BRIN), approval number 014/KE.02/SK/02/2023, February 2, 2023. The 7 week old C57BL/6 mice with ±20 g weight were obtained from PT. Biomedical Technology Indonesia. To develop a subcutaneous prostate cancer mice model, about 1×10^6 RM1 mice prostate cancer cell line suspension was diluted in the mixture 100 μL of PBS/Matrigel in 1:1 ratio. The mixture was injected via subcutaneous at the right flank of the mice. The tumour development was evaluated for two weeks post-injection by palpation and visual observation and used for ex vivo fluorescence imaging studies.

2.7. Ex vivo fluorescence imaging

The prostate cancer-induced mice (C57BL/6) (n = 3) were intravenously injected on tail vein with an individual dose of each fluorescent probe **BPF-01** or **BPF-02** (5.0 μM, 1:9 DMSO/water for injection 0.1 mL, v/v). Following 2 h post-injection, the animals were euthanised. Several major organs, including liver, stomach, lung, kidney, heart, spleen, intestine, muscle, skin, and tumour were collected, and their fluorescence intensity was recorded using the optical imaging system, Berthold NightOWL LB 983 NC100 with the excitation and reception wavelengths of 475 and 510 nm, respectively. The images were captured and processed by using the V4.2 Living Imaging software, Caliper Life Sciences.

2.8. Radiolabelling

Labeling of fluorescent probes **BPF-01** and **BPF-02** with β^-/γ radionuclide (iodine-131) was accomplished under a low pH reaction conditions (pH = 5–6) using a previously reported direct radioiodination procedure, with some minor variations [24]. Briefly, the probe **BPF-01**/**BPF-02** (1.0 mg) was dissolved in DMSO (200 μL), and then incubated with stirring for 1.0 min. Subsequently,

chloramine-T solution (1.0 mg) in 100 μL H_2O was gently transferred to the reaction, followed by slow addition of NaI-131 solution (±18.5 MBq). The reaction solution was then shaken using an incubation mixer for 30 min at 25 °C, 700 rpm. The 0.5 M $Na_2S_2O_5$ (100 μL) was added, and the mixture vortexed for another 1 min to produce the radiolabelled products **[^{131}I]-BPF-01** and **[^{131}I]-BPF-02**. The radiochemical purity was determined by radio-TLC using TLC-SG F60 paper chromatography (0.5 × 10 cm) using a mobile phase of DCM:MeOH (10:1, v/v). The first and following peaks on the chromatogram represent the product and remaining iodine, respectively. The radiochemical purity (RCP) of the radiolabelled probes was measured by dividing the radioactivity in each product with the total radioactivity on the TLC paper (expressed in percentage).

2.9. Cellular uptake

The LNCaP, MCF-7, and A549 cell lines were preincubated into 24 well plates overnight with 1×10^6 cells/well. After the cells were preincubated, the medium was eliminated, and the cells were rinsed with Hanks Balanced Salt Solution (HBSS) (Thermo, Cat.No. 14025092). Then, the cells were incubated with I-131 (control), **[^{131}I] BPF-01** and **[^{131}I] BPF-02** (±0.037 MBq/10 μL) in HBSS at 37 °C for 0.5 h, 1h, and 2h. After the incubation period, cells were rinsed using HBSS, and then lysed with 0.25 M NaOH (Supelco). The cell lysates were subsequently collected, and the radioactivity in cells was counted using the Automatic Gamma Counter (2470 Wizard2™, PerkinElmer). The cellular uptake results were determined by the following formula:

$$\%\ \text{Cellular uptake} = \frac{\text{Radioactivity value of cell lysate}}{\text{Radioactivity value of 0.037 MBq sample}}\ \text{x } 100\%$$

2.10. Computational analysis

The mitochondrial translocator protein (TSPO) was used as a target receptor for computational studies, and extracted from a published pdb-file, obtained from RCSB Protein Data Bank (PDB ID: 2mgy). All tested compounds (**7–12**) were built by Avogadro and then geometrically optimized using ORCA (freeware) by utilising B3LYP Density Functional Theory approach with 6–31 basis set. AutodockTools 1.5.6 was used in preparing receptor and ligands input files for docking simulation. The grid box covered Ala23, Val26, Ser41, His43, Leu49, Ala110, Asp111, Trp143, Ala147, and Asn151 was considered as binding pocket. The initial conformation of ligands was obtained by docking simulation using Autodock Vina (freeware). To determine the best conformation of ligands on the flexible receptor, molecular dynamic simulations were performed using AMBER 20 (licensed purchased by BRIN) for 200ns at 310K. Visualizations of stable conformation and interaction were rendered employing UCSF Chimera and BIOVIA Discovery Studio (freeware).

2.11. Magnetic bead (specificity) study

The specificity of the probes was investigated by a magnetic bead experiment, following a general procedure outlined by Sharma et al. [25] and Pillarsetty et al. [26]. The study was divided by 2 groups (n = 4). The nonspecific binding of the **[^{131}I] BPF-01** or **[^{131}I] BPF-02** to Ni-NTA magnetic beads without the TSPO protein was evaluated in the first group (control); and the second group was the specific binding of **[^{131}I] BPF-01** or **[^{131}I] BPF-02** to the human TSPO His-tagged recombinant protein. Briefly, a 20 μL of a Ni-NTA magnetic bead (Thermo Scientific, USA) was transferred into a LoBind microcentrifuge tube. Subsequently, the beads were washed with PBS supplemented 0.05 % Tween-20 (PBS-T), followed by a homogenisation in a vortex mixer for 5 s. The beads were transferred to a DynaMag™-2 magnetic rack (Thermo Scientific, USA) for 45 s. The supernatant was then discarded, and the beads were resuspended into 390 μL of PBS-BSA 1.0 %. For the second group, the beads were incubated with 1.0 μg of TSPO recombinant protein with a histidine tag (Abbexa; Cambridge, UK) for 15 min. Further, the beads were washed with PBS-T, incubated with 1.0 ng of radiolabelled **[^{131}I] BPF-01** or **[^{131}I] BPF-02** in PBS-BSA solution for 30 min, and rotated on a rotating mixer. Then, the supernatant containing unbound **[^{131}I] BPF-01** or **[^{131}I] BPF-02** was separated. In order to remove nonspecifically bound radioligands, the beads then rinsed twice with PBS-T. The radioactivity in each bead was determined using a gamma counter. The relative binding fraction was calculated by dividing the radioactivity value accumulated in the beads with the total radioactivity of the radiolabelled compound (expressed in percentage).

2.12. Statistical analysis

The statistical analysis was accomplished by GraphPad Prism (La Jolla, CA, USA, version 7.0) software. The statistical significance was measured by one-way analysis of variance (ANOVA), while the difference between two groups was measured using *t*-test ($P < 0.05$). The data is provided as mean ± SD, unless stated otherwise.

3. Results and discussion

3.1. Organic synthesis

The fluorescent probes **BPF-01** and **BPF-02** were synthesised using a four-step procedure (Scheme 1). The structure of the compounds was confirmed by IR, ^{1}H NMR, ^{13}C NMR, and HRMS. The synthesis of benzothiazole acid **2**, Boc-protected amine **5**, and free

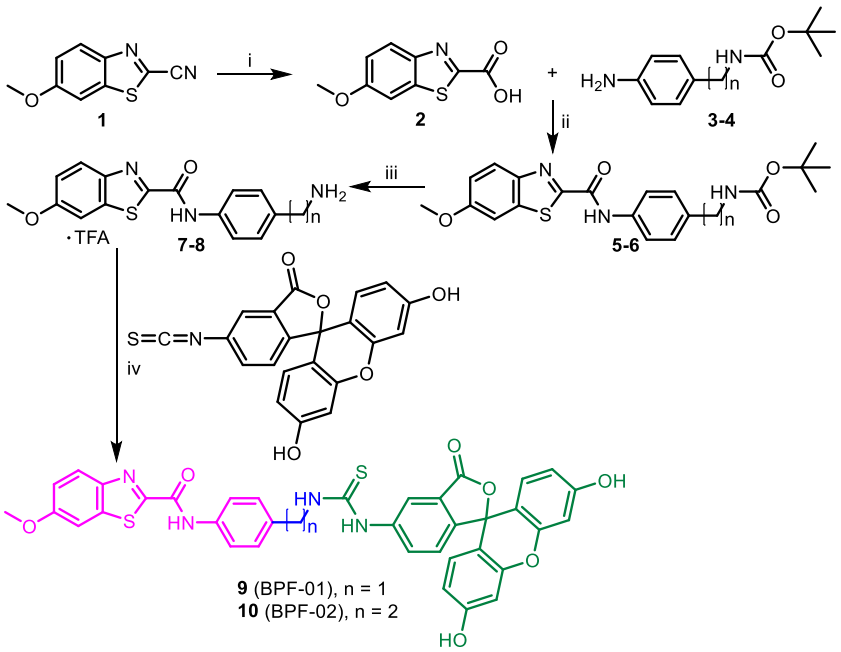

Scheme 1. Synthesis of fluorescent probes BPF-01 and BPF-02. (i) 1.0 N NaOH, EtOH, reflux, 18 h; (ii) DIPEA, HOBt, EDCl, DMF, rt, 18 h; (iii) TFA, CH_2Cl_2, rt, 8 h; (iv) DIPEA, DMF, 0 °C-rt, 18 h, N_2, in darkness.

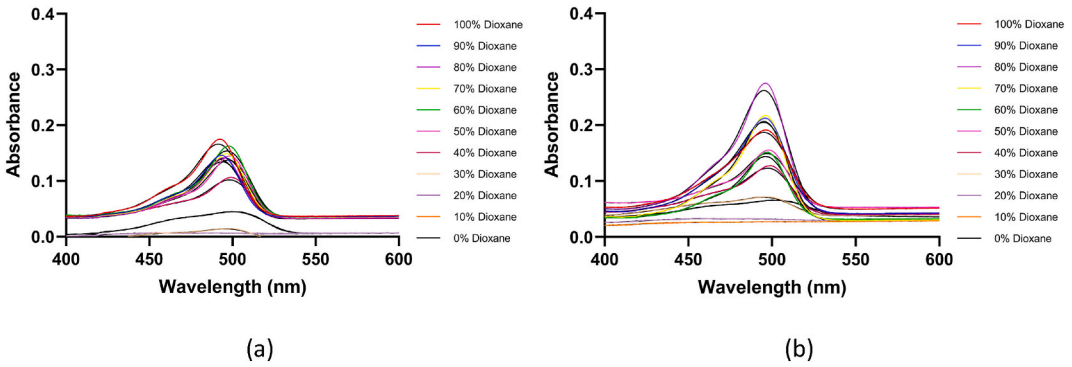

Fig. 1. The absorption spectra of fluorescent probes **BPF-01** (a) and **BPF-02** (b) at 10 μM in different solutions.

amine **7** were previously reported with good yields [21]. Briefly, acid **2** subsequently underwent amide coupling with amines **3**–**4** in the presence of EDCl, HOBt, and DIPEA to give Boc-protected amine **5**–**6** in 77 and 71 % yield, respectively. Boc deprotection of amines **5**–**6** with TFA in CH_2Cl_2 at rt for 18 h, followed by conjugation with FITC gave the fluorescent probes **BPF-01** and **BPF-02** with a respective yield of 52 and 57 % (Scheme 1).

3.2. UV–Vis spectra analysis

In the UV–Vis studies, spectroscopic properties of fluorescent probes **BPF-01** and **BPF-02** were investigated in different ratios of solvent system (dioxane:PBS) (0, 10, 20, 30, 40, 50, 60, 70, 80, 90, 100 %, v/v). In an aqueous solution, the spectrum of probe **BPF-01** (Fig. 1a) was characterised by an absorption maximum at around λ 500 nm which corresponds to the absorption of the FITC dye [27], showing an extinction coefficient (ε) of 3000 $M^{-1}cm^{-1}$. When the probe was dissolved in 50 % dioxane/PBS, the spectrum was characterised by an increase in the extinction coefficient ($\varepsilon = 14{,}500\ M^{-1}cm^{-1}$). A non-polar medium (100 % dioxane/PBS) promoted the improvement of extinction coefficient to 17,470 $M^{-1}cm^{-1}$. Similarly, the absorption maximum of probe **BPF-02** was also observed at around λ 500 nm (Fig. 1b). Overall, probe **BPF-02** exhibited higher extinction coefficients than probe **BPF-01**, suggesting that different lengths of carbon linker between the ligands and FITC moiety might influence the absorption properties. In 100 % PBS, the probe showed an ε of 6600 $M^{-1}cm^{-1}$. Dissolving the probe in 50 % dioxane/PBS promoted an improvement of the extinction coefficient to 15,560 $M^{-1}cm^{-1}$. As expected, increasing the ratio of non polar solvent (100 % dioxane/PBS) enhanced the extinction

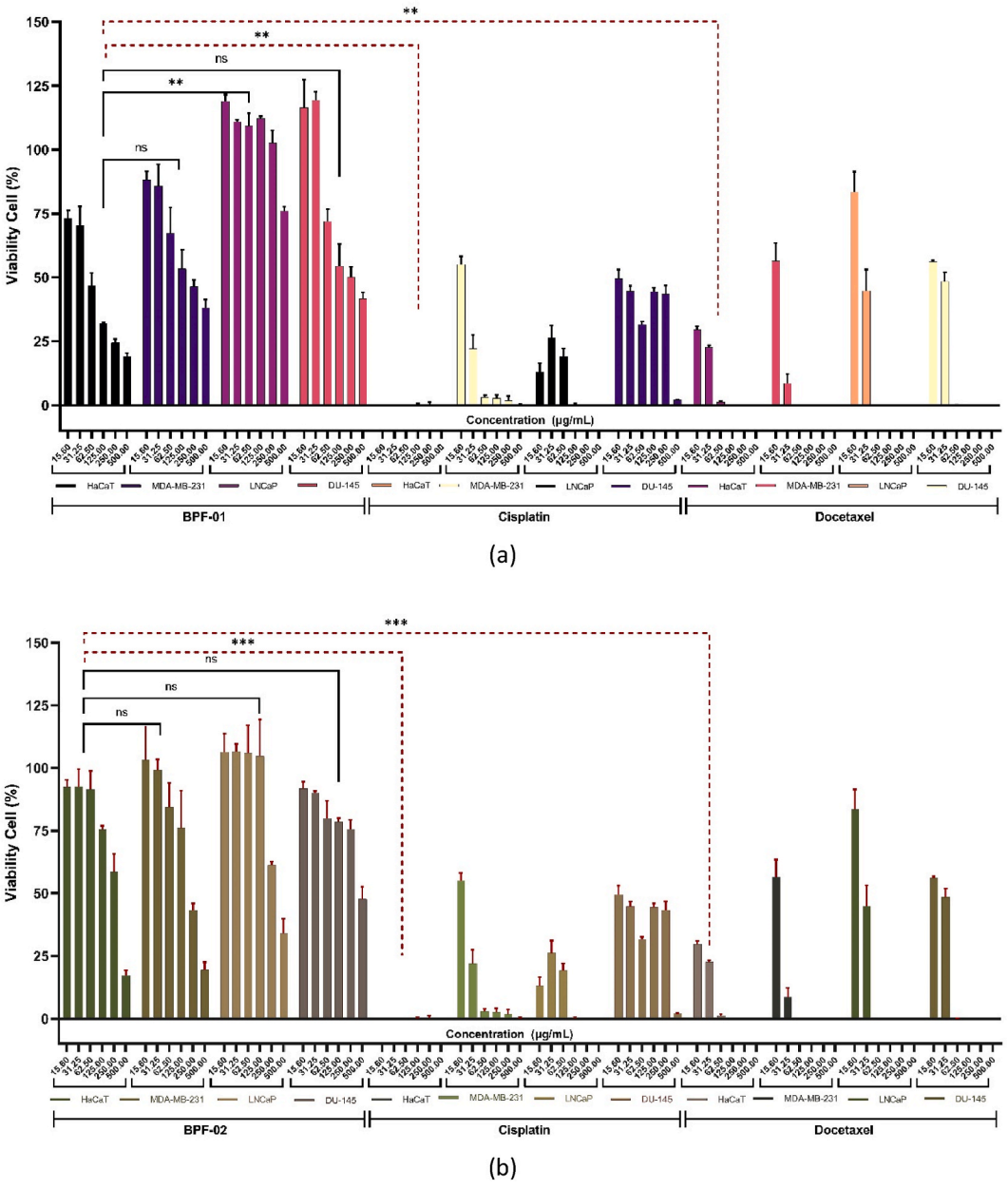

Fig. 2. Cell viability assays: Histograms represent the percentage of viable cells after the exposure of various concentrations of probes **BPF-01** (a) and **BPF-02** (b).

coefficient, with an observed ε of 19,140 $M^{-1}cm^{-1}$. However, the highest absorption of probe **BPF-02** was observed after dissolving the probe in 80 % dioxane/PBS, showing an ε of 27,495 $M^{-1}cm^{-1}$.

3.3. Biocompatibility and anticancer assays

MTT assay is the most common test used to measure the toxicity of treated compounds on the cells. Viable cells exhibit the capability to reduce a yellow water-soluble MTT dye to an insoluble purple crystallized formazan salt [28]. Cytotoxicity is evaluated using various measures based on cell and culture morphology (qualitatively), quantitative evaluation of cell damage, such as impacts on cell growth (proliferation), and certain features of cell metabolism [29]. In the present study, the biocompatibility of fluorescent probes **BPF-01** and **BPF-02** was evaluated by in vitro MTT assay using a normal immortalized human keratinocytes cell line (HaCaT). The results indicated that both probes relatively have low cytotoxicity in the concentration ranges of 0.0156–0.5 mg/mL as compared to anticancer drugs, cisplatin and docetaxel (control groups) (Fig. 2). Probe **BPF-01** showed more than 50 % cell viability at dose of

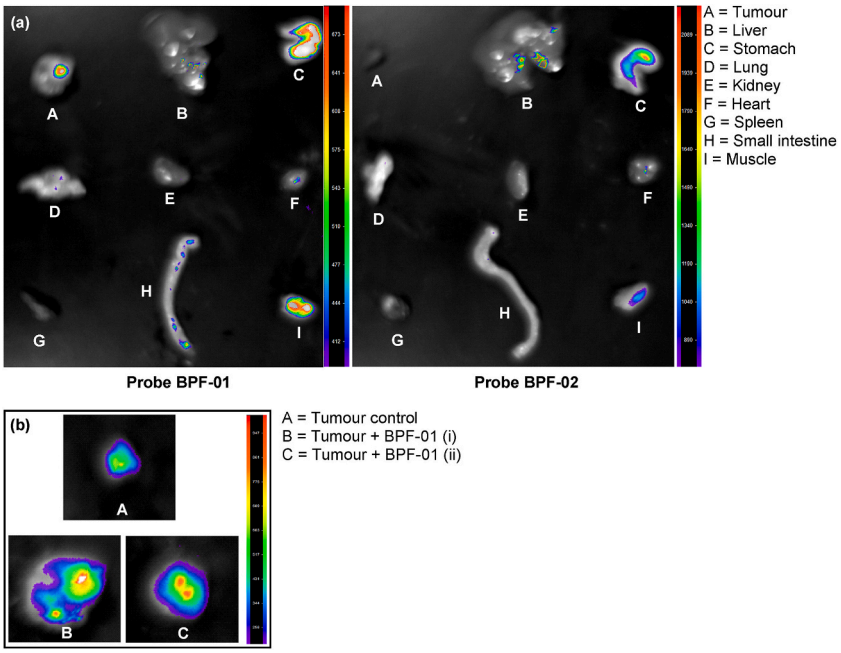

Fig. 3. Ex vivo fluorescence imaging of major normal organs and tumour tissues from prostate cancer-bearing mice using probes **BPF-01** and **BPF-02** (a), and imaging of tumour tissue (control) and tumour after injection of probe **BPF-01**: Panel A (tumour control), Panel B (tumour from mouse 1 after injection of the probe), and Panel C (tumour from mouse 2 after injection of the probe) (b).The mice used in (b) was different from (a).

≤0.03125 mg/mL (Fig. 2a), while more than 50 % cell viability after treatment with probe **BPF-02** was observed at dose of ≤0.25 mg/mL (Fig. 2b). At the highest concentration (0.5 mg/mL), both probes exhibited more than 18-fold cell survival than cisplatin and docetaxel.

Furthermore, the anticancer potency of **BPF-01** and **BPF-02** at various concentrations was assessed in several types cell lines: MDA-MB-231, LNCaP, and DU-145 after 24 h of treatment (Fig. 2). Although a dose-dependent reduction in cell growth was indicated in all cells, both probes displayed considerably low inhibition of cell growth compared to the positive control groups (cisplatin and docetaxel), as indicated by the high values of cell survival, especially in the LNCaP cells. At a high concentration (0.5 mg/mL), all cell models showed a reduction in viability of more than 50 % for both probes **BPF-01** and **BPF-02** (Fig. 2a and b), except in the LNCaP group treated with **BPF-01** (Fig. 2a). Following treatment with cisplatin and docetaxel, all cell types undergo morphological changes when observed through an inverted microscope. Nonetheless, after treatment with both probes (especially at 0.0156 mg/mL), the cell shape remains identical to that of the control cell (Supplementary Information S5). This is consistent with cell viability data showing that the probes have lower cytotoxicity than cisplatin and docetaxel. Since probes **BPF-01** and **BPF-02** were designed as molecular probes for the purpose of cancer imaging (diagnostic), they do not necessarily display good anticancer properties. To futher evaluate the biocompatibility of the probes, in vivo toxicity studies using normal mice and cancer-induced mice will be performed in future works.

3.4. Ex vivo fluorescence imaging

The feasibility of the synthesised probes for image-guided surgery was mainly determined by their capability to accumulate in cancer tissues either by active or passive targeting. In the present study, we initally synthesised two fluorescent probes **BPF-01** and **BPF-02**, and further evaluated their feasibility to target cancer by ex vivo fluorescence imaging. The specific objective of this experiment was to explore the potential use of the probes for fluorescence image-guided surgery, especially in the process of (1) tissue biopsy examination to discriminate normal cells from tumour cells and (2) ex vivo imaging to investigate pathological specimens. These two sub-procedures will enable the visualisation of potentially tumour-harboring margins in need of further clinical assessment.

To assess the accumulation of the fluorescent probes **BPF-01** and **BPF-02** in tumour tissues, we performed the fluorescence imaging ex vivo in the syngeneic prostate cancer (RM1)-induced mice (Fig. 3). After 3 h of intravenous injection of the probes, the mice were euthanised, and some major organs were collected and then imaged. The results demonstrated an accumulation of **BPF-01** in tumour compared to the control. Nevertheless, it seems that probe **BPF-02** was not able to accumulate in tumour tissue, as suggested by no appearance of the fluorescence signals in the observed area. Furthermore, it was observed that both probes exhibited minimum accumulation in several major organs. The relatively high fluorescence signals in the stomach may be due to background auto-fluorescence from the residue of the mouse diet [30], whereas the fluorescence signal in the muscle can be caused by hemoglobin autofluorescence [31].

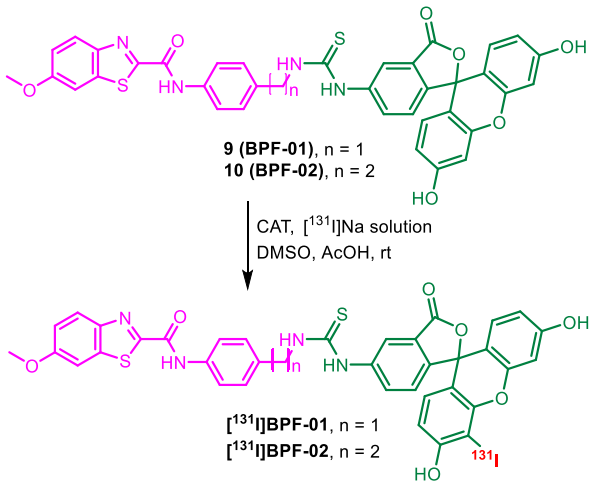

Scheme 2. Radiosynthesis of hybrid probes **[^{131}I] BPF-01** and **[^{131}I] BPF-02**, and the proposed outcomes.

It is worth noting that the accumulation of the probes can be affected by the physicochemical properties of the probes (molecular structures), and biological properties of the tumour, such as microvasculature density and interstitial fluid pressure. It has been found that large tumours contain fewer microvessels than small tumours [32]. Therefore, the accumulation of the probes might be strongly associated with the progression of tumour size and tumour stages, which highly depend on the individual animal responses. This could be the reason for the difference of the accumulation of BPF-01 as outlined in Fig. 3a and b (B), and Fig. 3b (C). In addition, the difference in molecular structures (length of the carbon linkers between ligands and FITC) could also influence their transport and uptake into the tumour tissues. Accordingly, despite **BPF-02** was not observed in tumour tissues after 3 h of intravenous injection, it is important to further investigate the accumulation of this probe before and after 3 h of treatment as well as explore other potential treatment routes (e.g., intraperitonial, intramuscular).

Although the use of optical fluorescence imaging offers sensitive detection of probe accumulation and has become a well-established modality for in vivo and ex vivo imaging of small animals, other alternative methods, such as flow cytometry and HPLC will be beneficial in providing supplementary data of the probe accumulation. The main advantage of flow cytometry and HPLC is their capability to detect and analyse probe accumulation inside cells. Another potential limitation of the current study is the probe accumulation was observed at one-single time point (3 h after the intravenous injection). Since the probe accumulation could be time-sensitive, further experiments using shorter (below 3 h post-injection) and longer (more than 3 h post-injection) time points for up to 24 h, is required in future works.

3.5. Radiolabelling

In this study, we successfully radioiodinated probes **BPF-01** and **BPF-02** to produce the hybrid probes **[^{131}I] BPF-01** and **[^{131}I] BPF-02**, respectively, with the chloramine T method. Iodine-131 with a half-life of 8.02 d emits both gamma and beta emitters, which exhibits potential for both therapeutic and diagnostic purposes [33,34]. Hence, this radionuclide was employed as a radioactive reporter for the development of hybrid probes in this study. The radioiodination of **BPF-01** and **BPF-02** was accomplished by substituting the hydrogen atom adjacent to phenol functionality at the FITC unit with an iodine atom via an electrophilic substitution mechanism [35], thus the chemical structure of **[^{131}I] BPF-01** and **[^{131}I] BPF-02** were proposed (Scheme 2). However, to some extent, di-iodination may also occur at the FITC moiety as suggested by a previous report [36]. Based on radio TLC analysis, the radiochemical purity of 93.37 and 96.5 % were obtained for hybrid probes **[^{131}I] BPF-01** and **[^{131}I] BPF-02**, respectively. We observed the peaks corresponding to the hybrid probes at Rf of 0.0–0.2, separated significantly from the unreacted [^{131}I]Na at R_f of 0.6–1 (Supplementary Information S6).

3.6. Cellular uptake

The uptake of control iodine-131, and **[^{131}I] BPF-01** and **[^{131}I] BPF-02** in studied cells was evaluated in three types of cancer cell lines in a time-dependent fashion. In-line with ex vivo fluorescence experiment, we used LNCaP cells for cellular uptake studies. We also performed the study on two additional cell lines, MCF-7 and A549. Previous research have identified that those three cells exhibited a high level of TSPO expression. Thus, this experiment will be beneficial in providing preliminary data on the capability of the probes to accumulate via active targeting by binding to the TSPO.

In the MCF-7 cell line, the **[^{131}I] BPF-01** showed a rapid increase in cellular accumulation after 0.5 h of incubation (9.67 ± 2.03 %); around 4-folds higher than iodine-131 (2.32 ± 0.81 %) ($p < 0.01$). The cellular uptake increased until 2 h post incubation (16.11 ± 1.52 %) ($p < 0.001$). Meanwhile, the cellular accumulation of **[^{131}I] BPF-02** on MCF-7 was considerably low and showed no significant

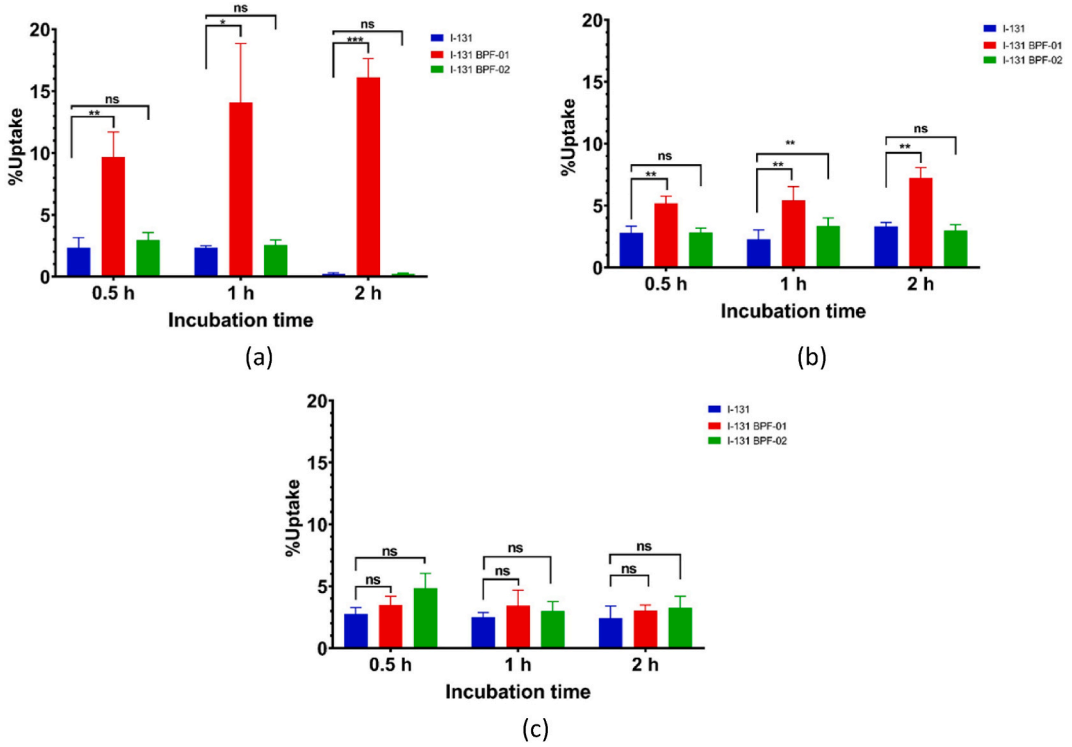

Fig. 4. Cellular uptake analysis of iodine-131 (control), **[^{131}I] BPF-01**, and **[^{131}I] BPF-02** in MCF-7 (a), A549 (b) and LNCaP (c) cell lines at 0.5 h, 1 h, and 2 h after incubation (n = 4). Significant differences between iodine-131 (control), **[^{131}I] BPF-01**, and **[^{131}I] BPF-02** in various time-points were indicated as $*p < 0.05$, $**p < 0.01$ and $***p < 0.001$.

difference with iodine-131 (Fig. 4a). The cellular uptake performed on lung cancer cells using A549 revealed an increased uptake of **[^{131}I] BPF-01** when compared to iodine-131. The uptake values were relatively constant (above 5.00%) with respect to the incubation time, where at 2 h of post-incubation a significant uptake was obtained (7.23 ± 0.84%); around 2-fold higher than iodine-131 (3.33 ± 0.31%) with $p < 0.01$. On the other hand, the uptake values of **[^{131}I] BPF-02** were low and showed similar values with iodine-131 uptake. It was identified that uptake only increased from 0.5 h to 1 h of incubation, and decreased at 2 h, which was not significant when compared to iodine-131 (Fig. 4b). In addition, the cellular uptake assay was performed on LNCaP cells as a prostate cancer model. The results showed that there was no significant uptake over 2 h of incubation time for both **[^{131}I] BPF-01** and **[^{131}I] BPF-02**. Although both probes demonstrated slightly higher uptake than iodine-131, no statistically significant difference between the groups was observed (Fig. 4c).

As suggested by cellular uptake assays, the hybrid radio-fluorescent probe **[^{131}I] BPF-01** demonstrates a promising property for its potential use as a molecular probe targeting cancer and/or more specifically targeting molecular receptors involved in the progression of cancer cells. The probes displayed a significant uptake by the MCF-7 and A549 cells, and therefore could be a strong candidate for a dual-imaging agent during the surgery of breast and lung cancers. We hypothesise that **[^{131}I] BPF-01** uptake could be the result of passive diffusion due to enhanced cancer cell permeability and retention (passive targeting) and/or binding of the probe with the receptor (s) overexpressed in cancer cells (active targeting) [37,38]. To date, the development of fluorescence substances for surgical guidance of solid tumours, such as breast cancer, has been extensive, and has led to promising preclinical results, as exemplified by several fluorescent probes, such as the H3-PEG2k compound based on NIR-II fluorescence imaging [39] and methylene blue (MB) based for ex vivo procedures [40]. Moreover, some hybrid probes have been developed for image-guided surgery of solid tumours, including [^{68}Ga]-SCH2 [41], [^{111}In]-DOTA-girentuximab IRDye800CW [42], and [^{68}Ga]-IRDye800CW-BBN [43].

It is worth noting that molecular structures of **BPF-01/BPF-02** and **[^{131}I] BPF-01/[^{131}I] BPF-02** are different. The presence of iodine atom in **[^{131}I] BPF-01** and **[^{131}I] BPF-02** could influence the absorption, distribution, metabolism, and excretion (ADME) of these probes in the biological system, and therefore affect their in vivo/in vitro accumulation. Therefore, this may cause the difference in uptake/accumulation patterns during ex vivo fluorescence imaging (**BPFs**) and cellular uptake studies (radioiodinated **BPFs**) on LNCaP cells/prostate cancer. In addition, since the circulation of blood into the tumour cells is closely associated to tumour vascularisation, the size and stages of tumour development play important roles in determining probe accumulation. Therefore, it is anticipated that the degree of probe accumulation in animals (in vivo/ex vivo) may not always be linearly correlated with their accumulation in in vitro settings.

Table 1
The binding affinity of compounds **7**–**12** on the TSPO receptor.

Compounds name	Binding affinity (kcal/mol)	Key Residues
12 (**[^{131}I] BPF-02**)	−21.6	Val 26, Ala 110, Ala 23, Leu 49, Trp 107, Trp 95, Leu 114, Trp 143, Gly 19, Asp 111
11 (**[^{131}I] BPF-01**)	−21.7	Val 26, Ala 23, Arg 46, Leu 49, Trp 107, Trp 95, Gly 19, Hie 43, Asp 111
10 (**BPF-02**)	−21.7	Val 26, Arg 46, Leu 49, Trp 107, Leu 150, Hie 43
9 (**BPF-01**)	−22.4	Val 26, Ala 110, Trp 143, Leu 150, Hie 43, Asp 111
8	−10.8	Ala 110, Arg 46, Gly 19
7	−10.6	Val 26, Ala 110, Ala 23, Leu 114

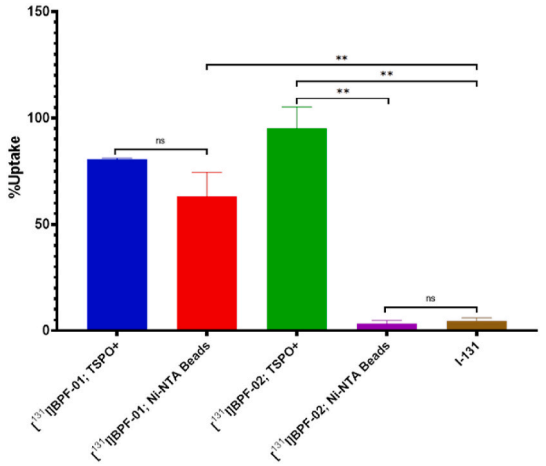

Fig. 5. Specific recognition of **[^{131}I] BPF-01** and **[^{131}I] BPF-02** to human TSPO protein. Significant differences among groups are indicated as $^{**}p < 0.01$.

3.7. Computational analysis

Docking simulations of the optimized compounds **7**–**8** into the TSPO binding pocket site were performed. TSPO receptor was selected as a cancer biomarker to evaluate the targetability of the synthesised probes for cancer cells because this receptor has been reported to be linked with the pathogenesis of a variety of solid cancers, such as breast, lung, and prostate cancers, in which its expression seems parallel with the disease progression. Moreover, a broad range of small molecules and bioconjugates have been synthesised as ligands to target the TSPO, some of which have been used in clinical studies either as imaging probes (fluorescent probes and radiotracers) or therapeutic agents [44–47]. More recently, an early effort has been made by Cohen et al. to target the TSPO for the purpose of image-guided surgery [48].

Fig. 6a showed that a small binding pocket is occupied by the tested compounds. The addition of FITC (compounds **9**–**10**) promoted the transformation of the TSPO-compounds binding model, where the FITC unit replaced the BTA moiety on the binding pocket (Fig. 6b). Furthermore, the hybrid probes **9**–**12** displayed higher binding affinity than **7**–**8** due to the interaction between FITC and TSPO, however, the presence of iodine atom slightly reduced the binding scores. In general, the hybrid probes bind to the receptor predominantly by hydrophobic bonds. The root mean square deviation (RMSD) data showed that all ligands stable on the receptor's binding pocket (Fig. 6c), while the graph of RMSF illustrated that all receptor residues did not fluctuated much during the dynamic simulation (Fig. 6d).

Docking scores and protein residues that bind to ligands are displayed in Table 1. The visualisation of ligand best conformation and interaction profiles are shown in Fig. 7: compounds **7** (Figs. 7a), **8** (Fig. 7b), **BPF-01** (Fig. 7c), **BPF-02** (Fig. 7d), **[^{131}I] BPF-01** (Fig. 7e), and **[^{131}I] BPF-02**) (Fig. 7f).

3.8. Magnetic beads

The aim of the magnetic bead assay was to determine the reactivity and specific recognition of probes **[^{131}I] BPF-01** and **[^{131}I] BPF-02** to TSPO protein, as previously predicted using computational analysis (Section 3.9). The uptake of **[^{131}I] BPF-02** (95.23 ± 10.0%) was significantly higher compared to the uptake in the Ni-NTA magnetic beads as the control group (3.40 ± 1.4%) ($p < 0.01$). Moreover, the probe uptake was around 17-fold higher than iodine-131 (4.57 ± 1.4%). These suggest that the probe has reactivity to TSPO. On the other hand, probe **[^{131}I] BPF-01** exhibited an uptake value of 80.62 ± 0.5%, no statistically different from the uptake in the magnetic beads group (63.15 ± 11.4%) (Fig. 5). Although probe **[^{131I}] BPF-01** showed potential binding to TSPO, it also exhibitied binding toward Ni-NTA beads, and therefore further experiments, such as knocking out the TSPO gene in cancer cell lines

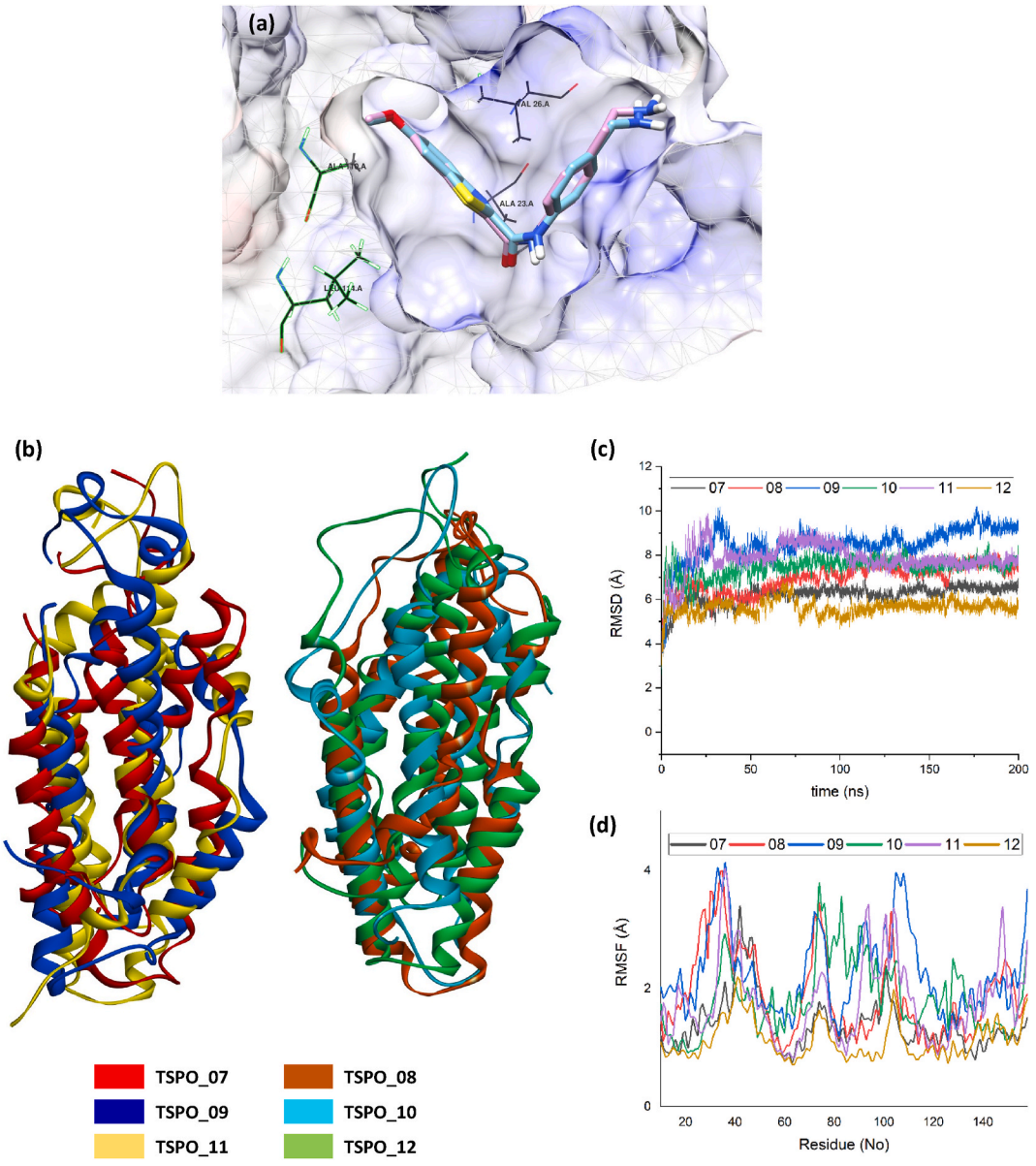

Fig. 6. Initial conformation of ligands **7** (blue) and **8** (purple) on the TSPO receptor resulted from molecular docking simulation (a), TSPO structures after molecular dynamics (b), RMSD (c), and RMSF (d).

and evaluating its uptake at different time points may be needed to confirm this data.

4. Conclusions

Recently, there is an increasing trend of combining radioactive and fluorescence imaging probes, serving as hybrid probes for translational applications. The use of hybrid radio-fluorescent probes designed to target solid tumours like breast and lung cancer in surgical procedures will be beneficial in enhancing tumour complete resection and verifying successful surgery, and thus increasing the patient's life expectancy. Over the past few years, several fluorescent probes bearing visible and near-infrared fluorophores have been developed to target cancers. In addition, the hybrid radioactive and fluorescence imaging technology has shown great potential for translational applications in oncology. In the present study, two new fluorescent probes **BPF-01** and **BPF-02**, and their corresponding radiolabelled probes, **[^{131}I]-BPF-01** and **[^{131}I]-BPF-02** have been synthesised and biologically evaluated. Ex vivo fluorescence study revealed that probe **BPF-01** seems to be accumulated in the cancer tissues of the prostate cancer mouse model. Furthermore, **[^{131}I]-BPF-01** showed considerably high uptake in the MCF-7 cell line when compared with the uptake in other cells (i.e., LNCaP and A549). Furthermore, the binding studies and computational analysis revealed that probes **BPF-01**, **BPF-02**, **[^{131}I]-BPF-01**, and **[^{131}I]-BPF-**

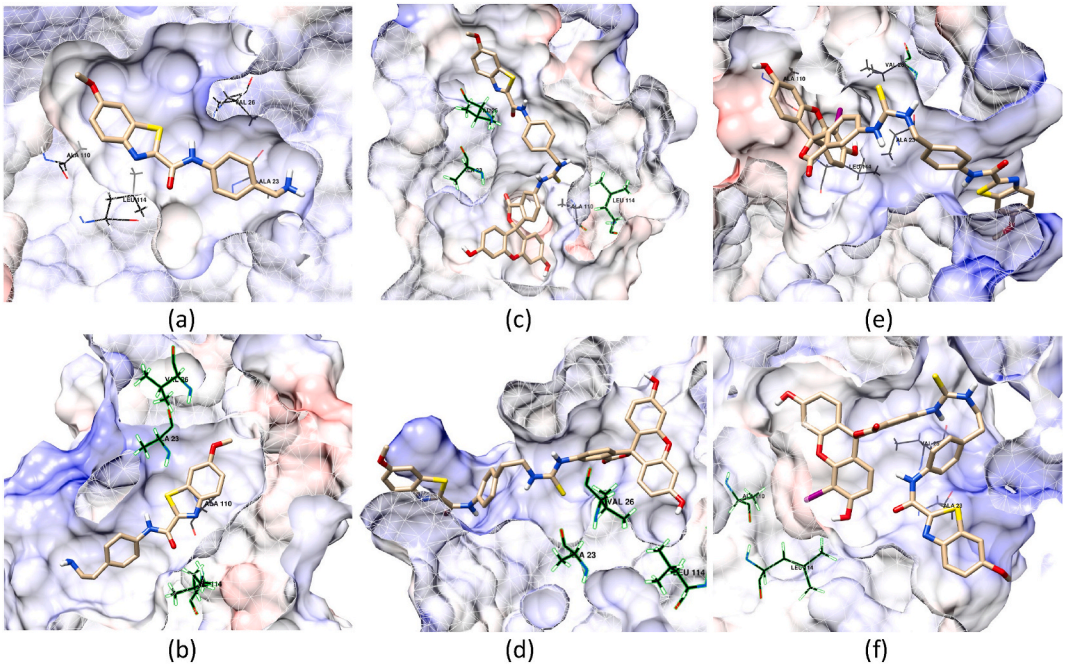

Fig. 7. Conformation and location of compounds **7** (a), **8** (b), **9** (BPF-01) (c), **10** (BPF-02) (d), **11** (**[^{131}I] BPF-01**) (e), and **12** (**[^{131}I] BPF-02**) (f) on the TSPO receptor.

02 showed the promising capability to target the TSPO receptor, which has recently been known as potential biomarkers for various solid cancers. Taken together, the synthesised fluorescent and hybrid probes demonstrated prospective applications to navigate the malignant cells during surgical tumour resection, although further studies, such as in vivo toxicity is needed to confirm the biocompatibility of the probes. Moreover, the accumulation of the probes can be time sensitive, and therefore further experiments using different time points up to 24 h after the injection are required to fully investigate their effectiveness and appropriate biomedical uses.

Data availability statement

Data included in article/supp. Material/referenced in article.

CRediT authorship contribution statement

Hendris Wongso: Conceptualization, Funding acquisition, Investigation, Methodology, Software, Supervision, Validation, Writing – original draft, Writing – review & editing. **Ahmad Kurniawan:** Formal analysis, Investigation, Methodology, Visualization, Writing – original draft, Writing – review & editing. **Alfian M. Forentin:** Formal analysis, Investigation, Methodology, Visualization, Writing – original draft. **Veronika Y. Susilo:** Formal analysis, Investigation, Methodology, Visualization, Writing – original draft. **Yanuar Setiadi:** Formal analysis, Investigation, Methodology, Visualization, Writing – original draft, Writing – review & editing. **Isa Mahendra:** Formal analysis, Investigation, Methodology, Visualization, Writing – original draft, Writing – review & editing. **Muhamad B. Febrian:** Formal analysis, Investigation, Methodology, Visualization, Writing – original draft. **Aziiz M. Rosdianto:** Investigation, Methodology, Resources. **Iwan Setiawan:** Investigation, Methodology, Resources. **Hanna Goenawan:** Investigation, Methodology, Resources. **Susianti Susianti:** Formal analysis, Investigation, Methodology, Resources. **Unang Supratman:** Investigation, Methodology, Resources. **Eva M. Widyasari:** Data curation, Investigation, Project administration, Formal analysis. **Teguh H. A. Wibawa:** Data curation, Formal analysis, Investigation, Project administration. **Maula E. Sriyani:** Data curation, Formal analysis, Investigation, Methodology. **Iim Halimah:** Data curation, Formal analysis, Investigation, Methodology. **Ronny Lesmana:** Investigation, Methodology, Resources.

Declaration of competing interest

The authors declare that they have no known competing financial interests or personal relationships that could have appeared to influence the work reported in this paper.

Acknowledgements

This work received funding from BRIN-Indonesia Endowment Funds for Education (LPDP) under the Research and Innovation Programme for "Indonesia Maju (RIIM)," (grant number 65/II.7/HK/2022). The authors acknowledge the facilities, scientific and technical support from Advanced Characterization Laboratories Serpong, National Research and Innovation Institute through E-Layanan Sains, BRIN. The computation in this work has been done using the facilities of MAHAMERU BRIN HPC, BRIN. The authors also thank the Directorate of Nuclear Facility Management, the radioisotope production team, our colleagues at the Multipurpose Reactor-G.A. Siwabessy and the Radioisotope Research Group (PRTRRB), BRIN for their support and generosity in providing radioactive material (iodine-131).

Appendix A. Supplementary data

Supplementary data to this article can be found online at https://doi.org/10.1016/j.heliyon.2023.e20710.

References

[1] X. Yi, F. Wang, W. Qin, X. Yang, J. Yuan, Near-infrared fluorescent probes in cancer imaging and therapy: an emerging field, Int. J. Nanomed. 9 (2014) 1347–1365.
[2] J. Haier, J. Schaefers, Economic perspective of cancer care and its consequences for vulnerable groups, Cancers 14 (2022) 1–19.
[3] J. Ferlay, M. Colombet, I. Soerjomataram, D.M. Parkin, M. Pineros, A. Znaor, F. Bray, Cancer statistics for the year 2020: an overview, Int. J. Cancer 149 (2021) 778–789.
[4] C. Chi, Y. Du, J. Ye, D. Kou, J. Qiu, J. Wang, J. Tian, X. Chen, Intraoperative imaging-guided cancer surgery: from current fluorescence molecular imaging methods to future multi-modality imaging technology, Theranostics 4 (2014) 1072–1084.
[5] D.T. Debela, S.G. Muzazu, K.D. Heraro, M.T. Ndalama, B.W. Mesele, D.C. Haile, S.K. Kitui, T. Manyazewal, New Approaches and Procedures for Cancer Treatment: Current Perspectives, vol. 9, SAGE Open Med, 2021, 20503121211034366.
[6] R. Baskar, K.A. Lee, R. Yeo, K.W. Yeoh, Cancer and radiation therapy: current advances and future directions, Int. J. Med. Sci. 9 (2012) 193–199.
[7] P. Debie, S. Hernot, Emerging fluorescent molecular tracers to guide intra-operative surgical decision-making, Front. Pharmacol. 10 (2019) 1–20.
[8] Y. Zheng, H. Yang, H. Wang, K. Kang, W. Zhang, G. Ma, S. Du, Fluorescence-guided surgery in cancer treatment: current status and future perspectives, Ann. Transl. Med. 7 (2019) 1–4.
[9] S. Tohme, R.L. Simmons, A. Tsung, Surgery for cancer: a trigger for metastases, Cancer Res. 77 (2017) 1548–1552.
[10] K.C. Cockburn, Z. Toumi, A. Mackie, P. Julyan, Radioguided surgery for gastroenteropancreatic neuroendocrine tumours: a systematic literature review, J. Gastrointest. Surg. 25 (2021) 3244–3257.
[11] R.P. Judy, J.J. Keating, E.M. DeJesus, J.X. Jiang, O.T. Okusanya, S. Nie, D.E. Holt, S.P. Arlauckas, P.S. Low, E.J. Delikatny, S. Singhal, Quantification of tumor fluorescence during intraoperative optical cancer imaging, Sci. Rep. 5 (2015), 16208.
[12] C.W. Barth, S.L. Gibbs, Fluorescence image-guided surgery - a perspective on contrast agent development, Proc. SPIE-Int. Soc. Opt. Eng. 11222 (2020) 1–26.
[13] F.W. van Leeuwen, R. Valdes-Olmos, T. Buckle, S. Vidal-Sicart, Hybrid surgical guidance based on the integration of radionuclear and optical technologies, Br. J. Radiol. 89 (2016), 20150797.
[14] R. Yuen, F.G. West, F. Wuest, Dual probes for Positron Emission Tomography (PET) and fluorescence imaging (FI) of cancer, Pharmaceutics 14 (2022) 1–22.
[15] M. Nahrendorf, E. Keliher, B. Marinelli, P. Waterman, P.F. Feruglio, L. Fexon, M. Pivovarov, F.K. Swirski, M.J. Pittet, C. Vinegoni, R. Weissleder, Hybrid PET-optical imaging using targeted probes, Proc. Natl. Acad. Sci. USA 107 (2010) 7910–7915.
[16] H. Wongso, R. Hendra, A.S. Nugraha, R. Ritawidya, I. Saptiama, C.E. Kusumaningrum, Microbial metabolites diversity and their potential as molecular template for the discovery of new fluorescent and radiopharmaceutical probes, Trends Anal. Chem. 159 (2023), 116900.
[17] T. Nagaya, Y.A. Nakamura, P.L. Choyke, H. Kobayashi, Fluorescence-guided surgery, Front. Oncol. 7 (2017) 1–16.
[18] U. Seibold, B. Wangler, R. Schirrmacher, C. Wangler, Bimodal imaging probes for combined PET and OI: recent developments and future directions for hybrid agent development, BioMed Res. Int. 2014 (2014), 153741.
[19] F.W.B. van Leeuwen, M. Schottelius, O.R. Brouwer, S. Vidal-Sicart, S. Achilefu, J. Klode, H.J. Wester, T. Buckle, Trending: radioactive and fluorescent bimodal/hybrid tracers as multiplexing solutions for surgical guidance, J. Nucl. Med. 61 (2020) 13–19.
[20] A. Irfan, F. Batool, S.A. Zahra Naqvi, A. Islam, S.M. Osman, A. Nocentini, S.A. Alissa, C.T. Supuran, Benzothiazole derivatives as anticancer agents, J. Enzym. Inhib. Med. Chem. 35 (2020) 265–279.
[21] H. Wongso, H. Goenawan, R. Lesmana, I. Mahendra, A. Kurniawan, T.H.A. Wibawa, W. Nuraeni, E. Rosyidiah, Y. Setiadi, N. Sylviana, Y.S. Pratiwi, A. M. Rosdianto, U. Supratman, C.E. Kusumaningrum, Synthesis and biological evaluation of new fluorescent probe bpn-01: a model molecule for fluorescence image-guided surgery, J. Fluoresc. 33 (2023) 1827–1839.
[22] A.E. Caprifico, E. Polycarpou, P.J.S. Foot, G. Calabrese, Biomedical and pharmacological uses of fluorescein isothiocyanate chitosan-based nanocarriers, Macromol. Biosci. 21 (2021), e2000312.
[23] T. Mosmann, Rapid colorimetric assay for cellular growth and survival: application to proliferation and cytotoxicity assays, Journal of lmmunological Methods 65 (1983) 55–63.
[24] H. Wongso, W. Nuraeni, E. Rosyidiah, Efficient and practical radiosynthesis of novel [^{131}I]-xanthine and [^{131}I]-hypoxanthine, At. Indones. 48 (2022) 185–191.
[25] S.K. Sharma, S.K. Lyashchenko, H.A. Park, N. Pillarsetty, Y. Roux, J. Wu, S. Poty, K.M. Tully, J.T. Poirier, J.S. Lewis, A rapid bead-based radioligand binding assay for the determination of target-binding fraction and quality control of radiopharmaceuticals, Nucl. Med. Biol. 71 (2019) 32–38.
[26] N. Pillarsetty, L.M. Carter, J.S. Lewis, T. Reiner, Oncology-inspired treatment options for COVID-19, J. Nucl. Med. 61 (2020) 1720–1723.
[27] S. Veeranarayanan, A.C. Poulose, S. Mohamed, A. Aravind, Y. Nagaoka, Y. Yoshida, T. Maekawa, D.S. Kumar, FITC labeled silica nanoparticles as efficient cell tags: uptake and photostability study in endothelial cells, J. Fluoresc. 22 (2012) 537–548.
[28] T.M. Alfareed, Y. Slimani, M.A. Almessiere, M. Nawaz, F.A. Khan, A. Baykal, E.A. Al-Suhaimi, Biocompatibility and colorectal anti-cancer activity study of nanosized $BaTiO_3$ coated spinel ferrites, Sci. Rep. 12 (2022), 14127.
[29] A. Bruinink, R. Luginbuehl, Evaluation of biocompatibility using in vitro methods: interpretation and limitations, Adv. Biochem. Eng. Biotechnol. 126 (2012) 117–152.
[30] S. Bhaumik, J. DePuy, J. Klimash, Strategies to minimize background autofluorescence in live mice during noninvasive fluorescence optical imaging, Lab. Anim. 36 (2007) 40–43.
[31] N.C. Whittington, S. Wray, Suppression of red blood cell autofluorescence for immunocytochemistry on fixed embryonic mouse tissue, Curr. Protoc. Neurosci. 81 (2017) 1–18.
[32] W. Zhan, W. Gedroyc, X.Y. Xu, The effect of tumour size on drug transport and uptake in 3-D tumour models reconstructed from magnetic resonance images, PLoS One 12 (2017), e0172276.

[33] T. Ferris, L. Carroll, S. Jenner, E.O. Aboagye, Use of radioiodine in nuclear medicine-a brief overview, J. Label. Compd. Radiopharm. 64 (2021) 92–108.
[34] J. Jeon, Review of therapeutic applications of radiolabeled functional nanomaterials, Int. J. Mol. Sci. 20 (2019) 1–17.
[35] S.A. Petrov, M.S. Yusubov, E.K. Beloglazkina, V.G. Nenajdenko, Synthesis of radioiodinated compounds. Classical approaches and achievements of recent years, Int. J. Mol. Sci. 23 (2022), 13789.
[36] C.A. Gabel, B.M. Shapiro, [^{125}1]Diiodofluorescein isothiocyanate: use as a reagent for labeling cells to high specific its synthesis and proteins and radioactivity, Anal. Biochem. 86 (1978) 396–406.
[37] M.T. Olson, Q.P. Ly, A.M. Mohs, Fluorescence guidance in surgical oncology: challenges, opportunities, and translation, Mol. Imag. Biol. 21 (2019) 200–218.
[38] J. Wu, The enhanced permeability and retention (epr) effect: the significance of the concept and methods to enhance its application, J. Personalized Med. 11 (2021) 1–8.
[39] X. Zeng, L. Xue, D. Chen, S. Li, J. Nong, B. Wang, L. Tang, Q. Li, Y. Li, Z. Deng, X. Hong, M. Wu, Y. Xiao, A bright NIR-II fluorescent probe for breast carcinoma imaging and image-guided surgery, Chem. Commun. 55 (2019) 14287–14290.
[40] C. Zhang, D. Jiang, B. Huang, C. Wang, L. Zhao, X. Xie, Z. Zhang, K. Wang, J. Tian, Y. Luo, Methylene blue-based near-infrared fluorescence imaging for breast cancer visualization in resected human tissues, Technol. Cancer Res. Treat. 18 (2019), 1533033819894331.
[41] Y. Sun, X. Zeng, Y. Xiao, C. Liu, H. Zhu, H. Zhou, Z. Chen, F. Xu, J. Wang, M. Zhu, J. Wu, M. Tian, H. Zhang, Z. Deng, Z. Cheng, X. Hong, Novel dual-function near-infrared II fluorescence and PET probe for tumor delineation and image-guided surgery, Chem. Sci. 9 (2018) 2092–2097.
[42] M.C. Hekman, M. Rijpkema, C.H. Muselaers, E. Oosterwijk, C.A. Hulsbergen-Van de Kaa, O.C. Boerman, W.J. Oyen, J.F. Langenhuijsen, P.F. Mulders, Tumor-targeted dual-modality imaging to improve intraoperative visualization of clear cell renal cell carcinoma: a first in man study, Theranostics 8 (2018) 2161–2170.
[43] D. Li, J. Zhang, C. Chi, X. Xiao, J. Wang, L. Lang, I. Ali, G. Niu, L. Zhang, J. Tian, N. Ji, Z. Zhu, X. Chen, First-in-human study of PET and optical dual-modality image-guided surgery in glioblastoma using ^{68}Ga-IRDye800CW-BBN, Theranostics 8 (2018) 2508–2520.
[44] L. Zhang, K. Hu, T. Shao, L. Hou, S. Zhang, W. Ye, L. Josephson, J.H. Meyer, M.R. Zhang, N. Vasdev, J. Wang, H. Xu, L. Wang, S.H. Liang, Recent developments on PET radiotracers for TSPO and their applications in neuroimaging, Acta Pharm. Sin. B 11 (2021) 373–393.
[45] P. Singh, A. Adhikari, D. Singh, C. Gond, A.K. Tiwari, The 18-kDa translocator protein PET tracers as a diagnostic marker for neuroinflammation: development and current standing, ACS Omega 7 (2022) 14412–14429.
[46] C.J. Austin, J. Kahlert, M. Kassiou, L.M. Rendina, The translocator protein (TSPO): a novel target for cancer chemotherapy, Int. J. Biochem. Cell Biol. 45 (2013) 1212–1216.
[47] N.H. Bhoola, Z. Mbita, R. Hull, Z. Dlamini, Translocator protein (TSPO) as a potential biomarker in human cancers, Int. J. Mol. Sci. 19 (2018) 2176.
[48] A.S. Cohen, J. Li, M.R. Hight, E. McKinley, A. Fu, A. Payne, Y. Liu, D. Zhang, Q. Xie, M. Bai, G.D. Ayers, M.N. Tantawy, J.A. Smith, F. Revetta, M.K. Washington, C. Shi, N. Merchant, H.C. Manning, TSPO-Targeted PET and optical probes for the detection and localization of premalignant and malignant pancreatic lesions, Clin. Cancer Res. 26 (2020) 5914–5925.